Journal of Materials Chemistry B

ROYAL SOCIETY OF CHEMISTRY

PAPER

View Article Online
View Journal | View Issue

Cite this: J. Mater. Chem. B, 2024, 12, 1636

Quantification and biological evaluation of $Zn_xFe_{3-x}O_4$ nanoparticle stiffness in a drug delivery system of MCF-7 cancer cells†

Hamzah Al-madani, ‡[ab] Yiqian Yang,‡[ac] Moath Refat,[d] Qingxin He,[e] Hao Peng,[a] Aiguo Wu *[af] and Fang Yang *[af]

The delivery of nanoparticles (NPs) to tumors remains challenging despite significant advancements in drug delivery technologies. Addressing this issue requires the establishment of quantitative and reliable criteria to evaluate the cellular absorption of NPs. The mechanical characteristics of NPs and their interaction with cells play a crucial role in cellular drug delivery by influencing cellular internalization. In particular, NPs' stiffness has emerged as a key factor affecting cellular uptake and viability. In this study, we synthesized $Zn_xFe_{3-x}O_4$ NPs with varying Zn doping concentrations and conducted an extensive measurement process to investigate the impact of NP stiffness on cellular uptake and the viability of cancerous cells. Initially, the stiffness of the NPs was measured using two methods: single-molecule force spectrometry of atomic force microscopy (SMFS-AFM) and cation distribution as chemical structure analysis. The influence of NP stiffness on intracellular behavior was examined by assessing cellular uptake and viability at different time points during the incubation period. The results obtained from both stiffness measurement methods exhibited consistent trends. NPs with higher stiffness exhibited enhanced cellular uptake but exhibited reduced cellular viability compared to the lower-stiffness NPs. Our findings provide valuable insights into the influence of Zn doping concentration on the mechanical properties of $Zn_xFe_{3-x}O_4$ NPs and their consequential impacts on cellular internalization. This study contributes to an improved comprehension of the mechanisms underlying cellular uptake and facilitates advancements in the field of drug transport, thereby enhancing the efficiency of NP-based drug delivery.

Received 15th November 2023,
Accepted 15th January 2024

DOI: 10.1039/d3tb02723f

rsc.li/materials-b

1. Introduction

Nanoparticles (NPs) have a significant impact on drug delivery systems, but their efficient delivery to tumors remains challenging. Previous studies have reported low delivery efficiencies (nanoparticle biodistribution coefficients (NBC) in tumor = 3.4%ID per g),[1] indicating a need for reliable criteria to evaluate NPs' absorption by cells. Previous meta-analysis revealed that the median delivery efficiencies of NPs to solid tumors were around 0.7–0.76%ID of the injected dose.[2,3] Therefore, in the drug delivery and nanosafety evaluation field, there is a growing need for quantitative and reliable criteria to evaluate the cellular absorption of NPs.

NPs in the drug delivery industry encounter several difficulties that impose arbitrary and conflicting demands on their stiffness and shapes.[4] These obstacles include cellular uptake, tumor tissue penetration, and blood vessels. Cellular drug delivery is related to the physical and mechanical properties of NPs, as well as the cellular ability to sense external mechanical stimuli.[5] Cells can perceive mechanical cues and forces

[a] Ningbo Key Laboratory of Biomedical Imaging Probe Materials and Technology, Zhejiang International Cooperation Base of Biomedical Materials Technology and Application, Chinese Academy of Sciences (CAS) Key Laboratory of Magnetic Materials and Devices, Ningbo Cixi Institute of Biomedical Engineering, Zhejiang Engineering Research Center for Biomedical Materials, Ningbo Institute of Materials Technology and Engineering, Chinese Academy of Sciences, Ningbo 315201, P. R. China
[b] University of Chinese Academy of Sciences, Beijing 100049, P. R. China
[c] Department of Chemistry, College of Sciences, Shanghai University, Shanghai 200444, P. R. China
[d] Department of Biochemistry and Molecular Biology, The Key Laboratory of Environment and Genes Related to Disease of Ministry of Education, Health Science Center, Xi'an Jiaotong University, Xi'an 710061, P. R. China
[e] Guangxi Vocational & Technical Institute of Industry, Guangxi 530001, P. R. China
[f] Advanced Energy Science and Technology Guangdong Laboratory, Huizhou 516000, P. R. China. E-mail: aiguo@nimte.ac.cn, yangf@nimte.ac.cn

† Electronic supplementary information (ESI) available. See DOI: https://doi.org/10.1039/d3tb02723f

‡ H. A. and Y. Y. contributed equally to this work.

from their surroundings, inducing specific signaling pathways that control biological activities such as cellular spreading, proliferation, adhesion, and differentiation.[6] Drug delivery relies on NPs' mechanical properties and cellular sense, enabling them to adapt the levels, localization, and distribution of NPs within cells.[7] Due to their complexity, determining the appropriate physical characteristics for assessing NPs' cellular delivery, has been a topic of extensive discussion.[8] Therefore, a comprehensive understanding of the nanobiological interface is crucial for safe NP design and controlling their penetration, distribution, and clearance. Mechanobiological measurements are essential to investigating how NPs induce biomechanical alterations and influence the mechanical properties of cells, alongside assessing biological responses, resistance to therapeutic treatments, and the efficacy of drug delivery.[9]

Assessing the impact of nanoparticles on drug delivery efficacy requires measuring their mechanical properties alongside other physicochemical properties.[7] Understanding the influence of NPs on passive and active targeting is crucial for designing optimal nanocarriers. Previous research focuses on macroscopic interactions between cell–substrate, cell–cell, and cell–ligand interactions, but the extent of multi-parametric interaction remains unclear.[10]

These cellular-level *in vitro* investigations offer important details for understanding the overall effect of NPs.[10] The influence of NPs on cellular viability can be significantly altered by a variety of NPs characteristics, not just their chemical composition. Some parameters play important roles, such as size, shape, concentration, aggregation possibility, surface charge, and stiffness.[11,12]

The mechanical properties of NPs have been identified as crucial factors that influence cellular uptake, tumor tissue infiltration, subcellular transport, and toxicity.[13,14] The significant role of NP elasticity in regulating cell–NP interactions has been indicated by recent research using NPs with different mechanical properties. Studies have investigated the relationship between NP stiffness and cellular uptake and tumor penetrations.[3,5,7,8,13,15–23] Different stiffness values were examined for NPs of consistent shape, size, and surface, across various NP types. While stiffness variations were often the main factor influencing results, disparities in mechanical aspects like shape and size, as well as diverse synthesis methods, can introduce complexities into the evaluation of the impact of stiffness on cellular uptake and potentially confound the results.

In addition to investigating the influence of NP stiffness on cellular uptake, various cellular internalizations such as blood circulation lifetime, protein corona formation,[19] tumor accumulation and penetration, biodistribution,[20] antibody-mediated targeting, endocytosis and phagocytosis,[22] and accumulation in tumor tissues and blood vessels[23] have been extensively studied and characterized. Despite the importance of NP stiffness as a crucial factor determining cellular uptake and toxicity, a comprehensive exploration of stiffness measurement techniques is still lacking in current studies. Therefore, more effort must be put into creating accurate stiffness evaluation methods.

One of the most popular experimental methods for determining a NP's mechanical property is to measure the force required to bend it. Atomic force microscopy (AFM) is an alternative technique that can be used to examine the topology of the surface of NPs immobilized on a solid substrate as well as to measure the stiffness of NPs by scanning the sample surface with an AFM cantilever.[4,6] Its ability to operate effectively in physiological environments further enhances its popularity in this field.[24] Previous studies employed AFM to assess the changes in mechanobiology associated with differentiating NPs.[5,7,8,13–18,20,21,23,25–34] These studies have provided valuable insights into the impact of various mechanical properties of NPs, including size, surface coverage, stiffness, and shape on cellular behavior and internalization processes such as uptake, morphology, toxicity, and topography.[35]

AFM-enabled nanoindentation measurements are used to measure the NPs' softness using nano-size sensitive probes fabricated in the micro-cantilever.[20] By detecting and measuring the bending extent of the cantilever, AFM can achieve an effective elastic modulus with a few nanometers' resolution.[36] Nanoindentation AFM measurement has been utilized for the quantitative calculation and analysis of NP stiffness.[33,37]

Characterizing the relationship between Young's modulus and Zn-content (x) in nanoparticles (NPs) is complex, requiring analysis of fundamental chemical characters and separating material stress–strain behavior from NP geometry. Therefore, cation distribution as mechanical structure analysis has been used as an alternative method to evaluate NP stiffness.

However, a method based on the structural and Fourier transform infrared (FTIR) spectroscopy data parameter linked to elastic properties has been developed for exploring the stiffness with the other characteristics. The formation of the spinel phase has been established by FTIR and X-ray diffraction (XRD).[38] Through conducting various experiments and employing a series of mathematical operations, the elastic properties have been calculated for $Co_{1+x}Cr_xFe_{2-x}O_4$,[39] $Co_{1-x}Sr_xFe_2O_4$,[40] $Mn_{0.5}Zn_{0.5}Fe_{2-x}Al_xO_4$,[41] $CoFe_2O_4$,[42] $Co_{1-x}Zn_xFe_2O_4$,[43] $Mg_{0.5}Zn_{0.5}Y_xFe_{2-x}O_4$,[44] $Co_{1-x}M_xFe_2O_4$ (M = Zn, Cu and Mn),[45] $Co_{1-x}Zn_xFe_2O_4$,[46] $Zn_{0.5}Ni_{0.5}Al_xFe_{2-x}O_4$,[47] $Zn_{1-x}Co_xFe_2O_4$,[48] $NiAl_xFe_{2-x}O_4$,[49] $CuAl_xFe_{2-x}O_4$,[50] and $CoFe_2O_4$.[51]

Zinc-doped iron oxide nanoparticles ($Zn_xFe_{3-x}O_4$) were synthesized to improve their efficiency in biomedical applications such as in drug delivery carriers, magnetic resonance imaging (MRI), and magnetic hyperthermia for cancer therapy.[52,53] A comprehensive study on the doping mechanism within a specific concentration range (0.1, 0.2, 0.3, 0.4) for hydrophobic Zn-doped Fe_3O_4 NPs was conducted in our previous research. Fe^{2+}/Fe^{3+} are replaced by Zn^{2+} in the structure of Fe_3O_4, creating a stable state of $Zn_xFe_{3-x}O_4$ with a typical spinel shape. A better understanding of the mechanism of zinc doping in $Zn_xFe_{3-x}O_4$ NPs led to the identification of an ideal doping concentration for applications in MRI contrast imaging, which was determined to be x = 0.2.[53] Furthermore, significant theragnostic potential was later demonstrated for these Zn-doped Fe_3O_4 NPs, enabling magneto-mechanical therapies capable of selectively harming and ultimately eliminating

drug-resistant tumor cells.[37] Additionally, the impact of Zn^{2+} doping concentration on the lattice occupancy, magnetic characteristics, and photothermal effects of $Zn_xFe_{3-x}O_4$ NPs was investigated through the examination of dynamic changes in lattice structure, magnetic moment, and metal cation valence states.[54] Within the scope of these investigations on the doping process, we consider the ideal doping concentration (x) to be a crucial parameter.

In this comprehensive study, we synthesized $Zn_xFe_{3-x}O_4$ NPs with different concentrations of zinc doping and carried out a quantification measurement of NP stiffness, and studied their effect on cancer cellular internalization. To begin with, we utilized physical and chemical methods to measure the stiffness of the zinc-doped NPs across five doping contents (x = 0.1, 0.2, 0.3, 0.4, and 0.5). Two techniques were employed for stiffness measurement: nanoindentation using single-molecule force spectrometry of atomic force microscopy (SMFS-AFM) and cations distribution analysis using FTIR and XRD. We then assessed the effects of these samples with varying stiffness on cellular internalization, by evaluating MCF-7 cellular uptake and viability at different time points during the incubation period. The research highlights the connection between the mechanical characteristics of $Zn_xFe_{3-x}O_4$ NPs with varying Zn doping concentrations and cell internalization, thereby contributing to our understanding of drug delivery effectiveness.

2. Materials and methods

2.1 Materials

$Zn_xFe_{3-x}O_4$ NPs (x = 0.1, 0.2, 0.3, 0.4, and 0.5) were synthesized using a one-step hydrothermal method described elsewhere.[54] Briefly, the synthesis process involved dissolving $FeSO_4{\cdot}7H_2O$ and $Zn(Ac)_2{\cdot}2H_2O$ in deionized water, followed by the addition of citric acid and $N_2H_4{\cdot}H_2O$. The resulting solution underwent color changes and the formation of a precipitate. The reaction mixture was transferred into a Teflon-lined autoclave and subjected to high temperatures for several hours. After cooling normally at ambient temperature, the resulting precipitate was centrifuged to collect it. It was then cleaned with distilled water and ethanol before being dried by freeze-drying or refrigeration.

2.2 Characterization

High-resolution transmission electron microscopy HT7800 TEM (Hitachi, Japan) was used to analyze the morphologies of the produced $Zn_xFe_{3-x}O_4$ NPs and scanning electron microscopy with an SU8230 SEM (Hitachi, Japan). Prior to imaging, the samples were vacuum-treated using a Solarus II plasma cleaner (Gatan, USA). XRD patterns of the synthesized samples were taken with an AXS D8 X-ray diffractometer (Bruker, UK) with a Cu-Kα radiation source, performing at 40 kV, 300 K, and 40 mA. The crystal microstructure of the sample compounds was determined *via* Rietveld refinement using MDI Jade 6 software. Room temperature Infrared (IR) spectrometry was carried out using an IS50 FTIR Spectrometer (Thermo Fisher, USA) in the 400–4000 cm^{-1} range. Bulk density measurements were carried out with an AccuPyc II (Micromeritics, China).

2.3 SMFS-AFM measurement and analysis

The synthesized $Zn_xFe_{3-x}O_4$ NPs (x = 0.1, 0.2, 0.3, 0.4, and 0.5) were dissolved in 1 mL deionized water from Milli-Q (Millipore, USA) with a concentration of 1 $\mu g\ mL^{-1}$ and ultrasonicated for 20 min in an ultrasonic bath. Then, $Zn_xFe_{3-x}O_4$ NP solutions were dropped on a high smoothness surface. To avoid aggregation, the $Zn_xFe_{3-x}O_4$ NPs solutions were diluted 10 times and ultrasonicated again for another 20 min before dropping on the stainless-steel subsurface. Stainless-steel rectangular pieces (1 × 1 cm, roughness *ca.* 1 nm) were used as substrate surfaces after cleaning with chloroform and acetone and drying at room temperature. To ensure the $Zn_xFe_{3-x}O_4$ NPs were submerged in the subsurface, 30 minutes were waited after dropping the solution onto the substrate. The $Zn_xFe_{3-x}O_4$ NPs were then dried at 60 °C for 12 hours, after which the samples were vacuum-treated for 10 min using a Solarus II plasma cleaner (Gatan, USA) before being scanned with scanning electron microscopy using a SU8230 SEM (Hitachi, Japan). AFM was performed immediately following SEM while maintaining the sample in a vacuum chamber using a Solarus II plasma cleaner (Gatan, USA) – between the SEM and AFM scanning processes – to prevent air humidity and contamination from affecting the sample.

Multi-mode FastScan AFM (Bruker, USA) was chosen for the AFM measurements. Topological images and single-molecule force spectrometry (SMFS) were performed using a silicon-tip on nitride lever probe (Scansyst-air, Bruker, USA). The cantilever is triangular-shaped with a cone-shaped tip (spring constant k = 0.3 $N\ m^{-1}$). The spring constants of the probes were determined using the thermal tune method. Tapping mode (TM) was employed to acquire images of all samples. Subsequently, the obtained AFM images underwent flattening using NanoScope Analysis 1.8 software. The mechanical properties of individual $Zn_xFe_{3-x}O_4$ NPs were assessed by performing point-and-shoot measurements at specific locations using the captured images. This approach allowed for the evaluation of the mechanical characteristics of each NP individually. Separated $Zn_xFe_{3-x}O_4$ nanoparticles were randomly chosen from the topographic image after the area had been scanned. A crosshair on the image was then utilized to choose the precise position (on the top right of NPs) to collect the force curves. The indentation behavior of the surface was terminated by recorded force-indentation curves of the $Zn_xFe_{3-x}O_4$ NPs, and at the same time, a single force curve *versus* cantilever distance was captured. The Young's modulus was determined by analysis of the fitting force-indentation curves[55] (see the details in the ESI†). Accordingly, over 1000 curves for each sample were analyzed with MountainsLab 9 (Digital Surf, France) software.

2.4 Cell culture

The human breast cancer MCF-7 cells were obtained from the Cell Bank of the Chinese Academy of Sciences (Shanghai,

China). Cells were cultured in Dulbecco's Modified Eagle's Medium (DMEM) (Gibco), supplemented with 10% fetal bovine serum (Gibco) and 100 μg mL^{-1} penicillin. The cells were incubated at a standard temperature and under humidity conditions of 37 °C with 5% CO_2. When the cell density reached 80–90%, they were enzymatically digested and collected for subsequent experimental assessments.

2.5 Confocal microscope NP cellular uptake measurement

First, 1 mg mL^{-1} of $Zn_xFe_{3-x}O_4$ NPs (x = 0.1, 0.2, 0.3, 0.4, and 0.5) were mixed with a specific concentration of FITC dye and mechanically linked by electrostatic adsorption for 48 h. Simultaneously, the adherent MCF-7 cells were digested and detached with trypsin, and 1 mL of the cell suspension (1×10^5 cells per mL) was cultured in confocal dishes and incubated for 12 h under standard conditions at 37 °C and 5% CO_2. $Zn_xFe_{3-x}O_4$ NPs at FITC were prepared as a solution with 100 μg mL^{-1} concentration in fresh culture medium. The cell culture medium was replaced with 1 mL of freshly prepared solution and incubated for different time intervals at 4 h, 20 h, or 24 h. After the incubation, the medium was carefully sucked out, rinsed three times with PBS, and then paraformaldehyde (1 mL, PFA, 4%) was added and left for 30 minutes at 4 °C. After that, nuclear dye (Hoechst) was added to the dishes after the three PBS washes, and left for 30 minutes at 37 °C. Finally, cells in the confocal dishes were observed using a confocal laser scanning microscope (CLSM) (TCS SP8, Leica) for imaging. Among them, FITC (green) is excited at 488 nm, and its emission wavelength range is 515–540 nm, while Hoechst (blue) is excited at 405 nm and emits at 415–480 nm. All NP images were captured using a fluorescence microscope, employing consistent exposure settings. The subsequent analysis of the fluorescence microscopic images of the cells was conducted utilizing ImageJ software. The mean fluorescence intensity of the images was consolidated onto a single plane using the sum intensity, and cell outlines were manually traced. In order to facilitate the analysis, the projected area and total fluorescence intensity were quantified, with the calculation of ±SD and P-values using ANOVA.

2.6 Bio-TEM visualization during NP cellular uptake measurement

The cellular uptake of NPs was evaluated through Bio-TEM imaging sessions conducted at the Bio-ultrastructure Analysis Laboratory of the Analysis Center of Agrobiology and Environmental Sciences (Zhejiang University, China). The procedure involved seeding 1 mL of MCF-7 cells (50 000 mL^{-1}) into 24-well plates and incubating them for 24 h at 37 °C and 5% CO_2. Subsequently, the old culture medium was sucked out and rinsed three times with PBS, and then fresh medium was added containing $Zn_xFe_{3-x}O_4$ NPs (with x values of 0.2 and 0.5) at a concentration of 100 μg mL^{-1}. The cells were then incubated for 4, 20, and 24 h. After multiple washes with PBS, the cells were treated with trypsin, centrifuged, and exposed to 2.5% glutaraldehyde for 12 hours at 4 °C. Following fixation with a 1% citric acid solution, the samples were dehydrated using an ethanol gradient. Finally, the samples were processed for TEM analysis (Hitachi H-7650, Japan) by infiltration, embedding, slicing, staining, and observation.

2.7 NPs cellular viability measurement

The CCK-8 assay was used to evaluate the *in vitro* cellular viability of $Zn_xFe_{3-x}O_4$ (x = 0.1, 0.2, 0.3, 0.4, and 0.5) on MCF-7 cells at different concentrations (25, 50, 100, 200 μg mL^{-1}) after 4 h, 20 h, and 24 h. Briefly, in DMEM with 10% FBS, and 1% penicillin, cells were seeded in 96-well plates (1×10^4 cells per well) and allowed to adhere to the wells by incubating them at 37 °C and 5% CO_2 for 12 hours. Following two PBS rinses, Zn_xFe_{3-x}O4 NPs in fresh DMEM were introduced at different concentrations (25, 50, 100, 200 μg mL^{-1}) for different Zn_x doping (x = 0.1, 0.2, 0.3, 0.4, and 0.5). Following the initial treatment, the cells were further incubated for different time intervals of 4 h, 20 h, or 24 h. Subsequently, CCK-8 reagent (10 μL) was added to the cultures and further incubated for 1.5 h. Finally, a SpectraMax 190 microplate reader (Molecular Devices, USA) was used to measure the absorbance at 450 nm.

3. Results and discussion

3.1 Chemical structure analysis by cation distribution results and discussion

For the five zinc contents (x = 0.1, 0.2, 0.3, 0.4, and 0.5) of $Zn_xFe_{3-x}O_4$ NPs, the quantitative estimation of the Zn^{2+} doping concentration was carried out employing inductively coupled plasma optical emission spectrometry (ICP-OES) as stated in Table S1 of the ESI.† Fig. 1(a) illustrates the zinc-doped ferrite structure reordering the cation distributions. XRD patterns investigated the crystal structure of different samples of $Zn_xFe_{3-x}O_4$ NPs, as shown in Fig. 1(b). The diffraction peaks ((220), (311), (400), (422), (511), (440), (620), and (533)) were presented for different Zn doped content (x). Rietveld refinement confirmed that the synthesized NPs exhibit a single-phase cubic spinel structure with a space group of ($Fd\bar{3}m$).[38,54] Rietveld refinement shows that the average diameter of the crystallites is around 25 nm for all samples. Lattice constants were calculated using crystallite sizes and Miller indices, and they show increasing linearity with the Zn-content (x) from 8.3510 Å to 8.3772 Å. The bulk density (ρ_b) was measured and subsequently compared to the estimated X-ray density ($\rho_{XRD)}$, as shown in Fig. S1 in the ESI.† Porosity (P, %) and Poisson's ratio (σ) were determined depending on the X-ray density (ρ_{XRD}) and the bulk density (ρ_b), see the ESI,† for details. These parameters were documented as a function of various levels of Zn doping (x) in Table 1. FTIR spectrometry of different samples of $Zn_xFe_{3-x}O_4$ NPs with a wavenumber range of 400–900 cm^{-1} are shown in Fig. 1(c). Two absorption bands (ν_1) and (ν_2) are represented by the FTIR spectrometer, and they are listed in Table 2. The peaks (ν_1) arise from stretching the tetrahedral metal ion and oxygen bonding. These force constants are determined utilizing the Waldron relationship, represented by eqn (S3) and (S4) in the ESI.† Elastic constants

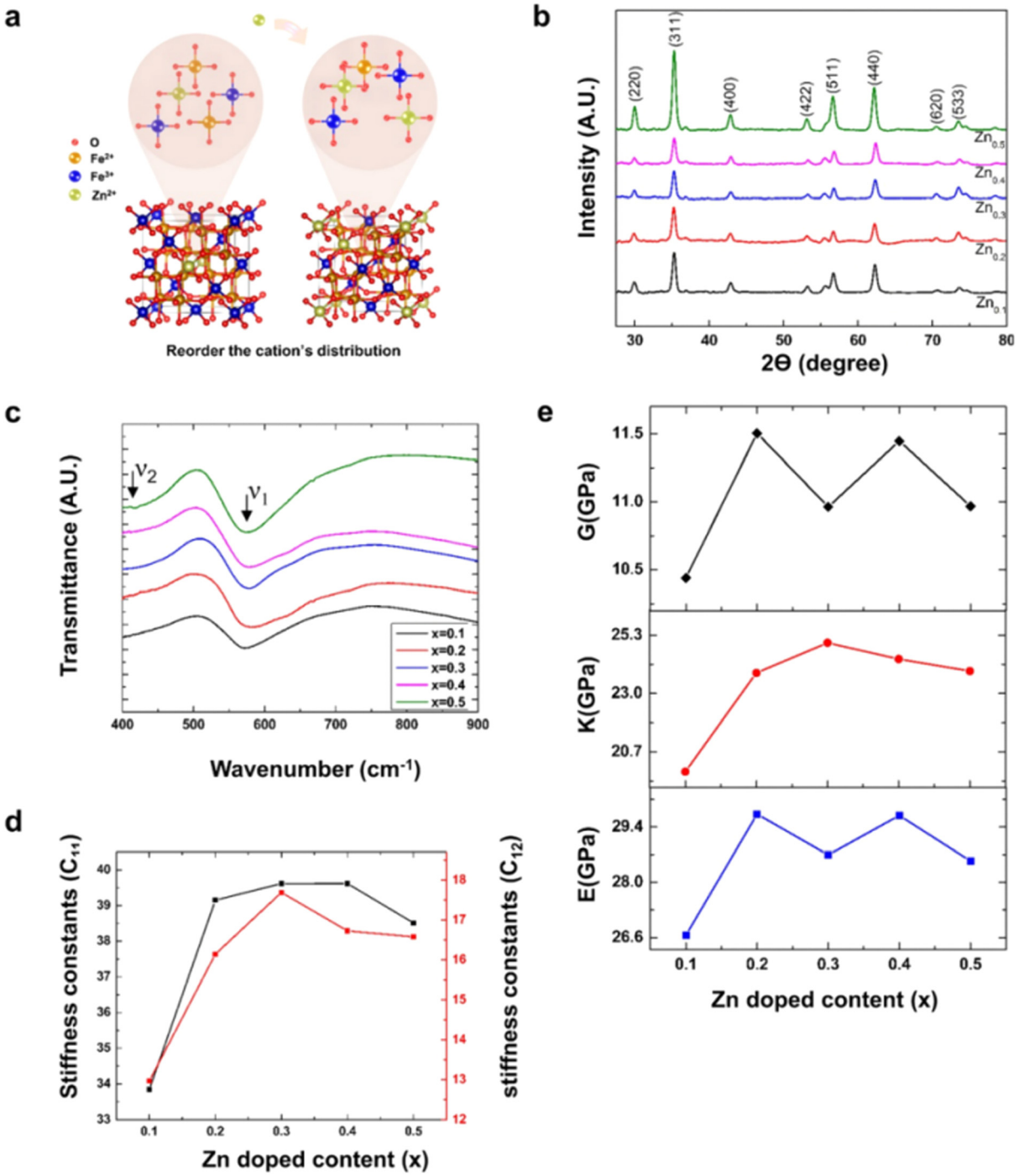

Fig. 1 NP stiffness evaluation by cation's distribution. (a) The atomic structure of the spinel zinc ferrite shows a difference in cation distribution with added Zn-doping content. The green, gold, blue and red atoms correspond to Zn, Fe^{2+}, Fe^{3+}, and O chemical elements, respectively. (b) FTIR spectra for $Zn_xFe_{3-x}O_4$ NPs at different Zn doping contents (x = 0.1, 0.2, 0.3, 0.4, and 0.5) in the 400–4000 cm^{-1} range. (c) XRD patterns of the crystal structure of $Zn_xFe_{3-x}O_4$ NPs at different Zn doping contents performed at 40 kV, 300 K, and 40 mA. (d) stiffness constants (C_{11}) and (C_{12}) at different Zn doping contents. (e) Young's modulus (E), bulk modulus (B), and rigidity modulus (G) at different Zn doping contents.

(C_{11}) and (C_{12}) are related to the force constants (k_o) and (k_t) and the Poisson ratio (σ).[39] (C_{11}) and (C_{12}) defined by eqn (S5)–(S7) in the ESI.† The calculated values of all these elastic constants with different Zn doped contents (x) are listed in Table 2 and graphically presented in Fig. 1(d) and (e) (details of the mathematical equations are listed in the ESI†).

Spinels are minerals with a cubic structure ($A^{2+}B_2{}^{3+}O_4{}^{2-}$), with oxide anions and cations "A" and "B" occupying octahedral and tetrahedral sites. Zn^{2+} ions occupy the tetrahedral "A" sites while Fe^{3+} ions occupy the octahedral "B" sites as bulk $ZnFe_2O_4$ crystallizes in the typical spinel structure. Nanoparticulate $ZnFe_2O_4$ exhibits soft ferrimagnetism due to significant

Table 1 Lattice parameter a_{XRD} (Å), crystallite size D (Å), X-ray density ρ_{XRD} (g cm^{-3}), true density ρ_b (g cm^{-3}), porosity P (%), and Poisson ratio σ for different samples of $Zn_xFe_{3-x}O_4$ NPs

x	2-Theta	D	a_{XRD}	ρ_{XRD}	ρ_b	P	σ
0.1	35.627	2.5179	8.351	5.1331	4.4188	0.1392	0.2770
0.2	35.596	2.5201	8.3581	5.1541	4.6652	0.0949	0.2919
0.3	35.556	2.5228	8.3671	5.1752	4.9407	0.0453	0.3087
0.4	35.514	2.5257	8.3767	5.1962	4.7786	0.0804	0.2968
0.5	35.519	2.5254	8.3757	5.2173	4.8606	0.0684	0.3009

randomization of cations.[56] Nano-zinc ferrites exhibit inversion and magnetization at ambient temperature, but bulk zinc ferrite is nonmagnetic in the micron regime.[41] Mixed ferrites' physical and chemical properties depend on cation stoichiometric spinel structures, which can be tuned through substitutions on either "A" or "B" lattice sites.[57] The complex magnetic behavior of magnetic NPs can be efficiently controlled using zinc (Zn),[54] a necessary trace element with favorable biocompatibility, increasing their potential for a variety of biological applications.[58] Therefore, understanding the physical properties of $Zn_xFe_{3-x}O_4$ spinel ferrite requires precise determination of its crystallographic structure.[59] Cation substitutions on the "A" or "B" lattice sites allow for fine-tuning of physical properties.[57]

According to studies,[6,25] fluctuations in the interatomic binding forces in the spinel lattice can be used to explain variations in the elastic moduli. The distance between interatomic bonds and the particular kinds of cations involved in their formation are two examples of variables that impact the strength of these binding forces. The distribution of cations in spinel ferrites is reflected in their IR spectra and impacts their elastic properties. The incorporation of Zn ions into Fe_3O_4 primarily occurs by replacing Fe ions, resulting in increased crystal spacing (d) and a lattice constant increase with Zn content (x). This increase follows the trend observed in previous literature[39,42–44,49,51] and obeys Vegard's Law.[46] The presence of pores generated during sample preparation can explain why the X-ray densities have been found to be greater than the equivalent bulk densities. Pores have a significant influence on bulk density. Additionally, increased Zn cation content leads to a higher X-ray density.

Unexpectedly, the results showed no correlation between porosity and Zn cations or grain size increase. Typically, intergranular porosity increases with grain size.[57] Therefore, this unexpected behavior results from the substantial instability in the bulk density associated with increasing Zn doped content (x) of $Zn_xFe_{3-x}O_4$. The significant instability in the bulk density can be further explained by the comparable mass densities of Zn^{2+} (7.14 gm cm^{-3}) and Fe^{3+} (7.86 gm cm^{-3}).[57] The Zn doped ferrite at (x = 0.3) has the highest bulk density equal to 4.9407 gm cm^{-3}, and the lowest porosity equal to 4.53%, whereas Zn doped ferrite (x = 0.1) has the lowest bulk density equal to 4.4188 gm cm^{-3} and the highest porosity equal to 13.92% as shown in Table 1. The uniform change in bulk density is attributed to differences in grain size, particularly irregular-shaped grains, and as the sintering process progresses.[44,56] Consequently, the movement of cations causes alterations in the mean ionic radii for octahedral and tetrahedral sublattices, affecting nearby ions' arrangement and interaction.[56] The presence of unexpected porosity has implicated Poisson's ratio, which provides valuable information about a material's bonding nature and ductile or brittle behavior.[42] Based on the Poisson ratio in Table 1, the different Zn doped content (x) exhibits a ductile nature (Poisson ratio $>$ 0.26).[39,42,56]

The higher absorption bands (ν_1) shift to higher values with increasing Zn doping (x), indicating a uniform change in the stretching of tetrahedral metal ions and oxygen bonding. However, the second absorption band (ν_2) shows an inconsistent change with increasing Zn doping content (x), suggesting that the cation-oxygen bonds in the octahedral location have irregular bending vibrations. By comparing the ionic radii of the substituted ions, we can gain insights into the explanation for this behavior. The ionic radius of Zn^{2+} is approximately 0.075 nm,[39] which is close to the ionic radius of Fe^{2+} at 0.076 nm,[60] but slightly larger than the ionic radius of Fe^{3+} at 0.064 nm.[59] The force constants (k_o) and (k_t), elastic constants (C_{11}) and (C_{12}), and elastic modulus (E), (B), and (G) showed unrelated changes with increasing Zn doped content (x). The observed variance in the results is attributed to the weakening of interatomic bonds resulting from the use of substituted metals.[42] Elastic moduli values are affected by the presence of porosities in the ferrite samples. The results for Young's modulus (E), as shown in Fig. 1(e), indicate the highest Young's modulus (E) corresponds to Zn doped content x = 0.2, while the lowest Young's modulus (E) is observed at Zn doped content x = 0.1.

3.2 SMFS-AFM stiffness measurement results and discussion

In the study of NP mechanical properties, the contact mode (or static mode) and single-molecule force spectrometry (SMFS) methods have been commonly employed, depending on the characteristics of NPs and the experimental conditions.[61] When

Table 2 The absorption bands ν_1, ν_2 (cm^{-1}) and force constants k_t, k_o (10^5 dyne m^{-2}), stiffness constants C_{11} and C_{12} (GPa), Young's modulus E (GPa), bulk modulus B (GPa), and rigidity modulus G (GPa) for different samples of $Zn_xFe_{3-x}O_4$ NPs

x	ν_1	ν_2	K_t	K_o	C_{11}	C_{12}	E	B	G
0.1	572.76	418.48	1.1605	4.4924	33.8457	12.9655	26.6634	19.9256	10.4401
0.2	581.44	422.82	1.8540	4.6906	39.1510	16.1427	29.7254	23.8122	11.5041
0.3	580.96	421.38	2.2666	4.3630	39.6172	17.6900	28.6958	24.9991	10.9636
0.4	578.07	423.31	2.5280	4.1098	39.6202	16.7259	29.6903	24.3573	11.4472
0.5	574.21	419.45	2.6992	3.7520	38.5042	16.5723	28.5312	23.8830	10.9660

an AFM cantilever interacts with NPs, force–distance (F–D) curves are generated, which represent the deflection of the cantilever as a function of distance.[62]

One of these significant mechanical properties discovered by AFM is stiffness, which is commonly defined as Young's modulus, which is a fundamental property of a material that describes the stress–strain relationship and characterizes its elasticity.[63] Higher modulus values indicate more stiffness, and it provides a quantifiable measurement of the stiffness.[36] The determination of Young's modulus, which reflects the material's elasticity, is influenced by various factors such as probe tip radius and half angle, probe spring constant, deflection sensitivity, and Poisson's ratio.[37]

In order to perform AFM-SMFS, isolating individual NPs and preventing aggregation is crucial. Accordingly, several steps were taken, including optimizing the particle dilution ratio in water, applying ultrasound, and confirming the locations of NPs through SEM imaging prior to measurements with AFM (see the details in the Materials and Methods section). Fig. 2(a) illustrates how the structure of the zinc-doped ferrite changes as the zinc content increases from $x = 0$ to $x = 0.5$. Fig. 2(b) and (c) show TEM and SEM images of $Zn_xFe_{3-x}O_4$ NPs at different doping contents, respectively. The TEM and SEM images clearly demonstrate the effectiveness of the employed procedures in isolating individual NPs and preventing their aggregation. This enables independent stiffness measurements for each particle, regardless of different Zn doping contents, while mitigating eternal influence that can compromise the validity of the measurements. The AFM topography images of $Zn_xFe_{3-x}O_4$ NPs at different doping contents are shown in Fig. 2(d). The AFM topography images were used to confirm NP sites and employed the point-and-shoot measurements. Since a conical tip was used, the Sneddon conical indenter model[64] was employed to fit the force-indentation curves and calculate the Young's modulus, see a detailed explanation in the ESI.†

Quantitative calculation of the elastic modulus of NPs requires an estimation of the Young's modulus by achieving the force-displacement curve (Fig. S3 in the ESI†) from the AFM deflection-displacement curve (Fig. S3 in the ESI†). We used an autorun template after bassline the AFM deflection-displacement curves for thousands of curves using MountainsLab 9 (Digital Surf, France) software to overcome this.

The statistical comparison of mean Young's modulus was determined using one-way ANOVA. The results, including the Gauss distribution of Young's modulus for each $Zn_xFe_{3-x}O_4$ NP sample, are shown in Fig. 2(e–i). Furthermore, our methodology uses the median value as the representative Young's modulus (E) value. This approach aims to mitigate the impact of a limited number of atypical modulus measurements illustrated for different Zn-content (x) of NPs in Fig. 2(j). Observing the provided figures, it is obvious that the Young's modulus does not directly correlate with the zinc content (x) of NPs.

According to Fig. 2(j), the highest Young's modulus is associated with a Zn-content of $x = 0.2$, while the lowest Young's modulus is connected to a Zn-content of $x = 0.1$. These results exhibit a similar trend to the values obtained using structure analysis by cation's distribution, as a function of Zn doping content (x).

A minor deviation in the application of force during AFM examination could affect the results by inducing horizontal movement or twisting the NPs. Despite efforts to apply the force precisely at the center of the NPs, an off-center force application could impact the obtained results. Extensive quantitative repetition was conducted to mitigate this, including testing numerous NPs and repeatedly testing a single NP, effectively minimizing the error level. In addition to defects, lattice strain, and bond energy, dislocations have also altered the mechanical properties of NPs.[65] The effect of NP size and indentation depth on the elastic modulus measured by AFM remains uncertain, necessitating further studies. The contact mechanics, including the frictional and mechanical behaviors of NPs, are not yet fully understood. Embedding three-dimensional NPs in polymeric matrices can lead to unique material properties, but the mechanical mismatch between particles and the matrix influences the overall response. Experimentally characterizing this effect at the nanoscale is complex due to the limited direct measurement methods available.[65]

3.3 Confocal microscopy of NP cellular uptake results and discussion

In order to investigate the impact of NP stiffness on their cancerous cellular uptake, the cellular uptake of various Zn doped content (x) was measured using a confocal laser scanning microscope (CLSM) (TCS SP8, Leica) after injection at different time points, including 4 h, 20 h, and 24 h.

The NPs began impacting the cells after 4 h but with different concentrations, and reached their peak effect after 24 h. A time period of 20 h was selected as an intermediate period before reaching the saturation state of cancerous cellular uptake.

MCF-7 cells were incubated with $Zn_xFe_{3-x}O_4$ NPs (x = 0.1, 0.2, 0.3, 0.4, and 0.5) for 4 h, 20 h, and 24 h and then observed by CLSM with excitation of Hoechst and FITC (more details can be found in the Materials and Methods section). Fig. 3 shows confocal microscope images of MCF-7 cells after uptake of different Zn doped content x at 4 h, 20 h, and 24 h.

Along the different time points, a stronger fluorescence of FITC in MCF-7 cells was observed after incubation with Zn doped content ($x = 0.2$) (the Zn-content associated with the highest Young's modulus), and the weaker FITC was observed at $x = 0.1$ (the Zn-content associated with the low Young's modulus).

Based on Fig. 3, fluorescence intensity increases with a prolonged incubation time of mixed FITC and different Zn doped content (x) with MCF-7 cells, indicating the enhanced cellular uptake of NPs over time. The impact of NP stiffness on cellular uptake was quantified by analyzing the mean fluorescence intensity at 4 h, 20 h, and 24 h for various levels of Zn-doped content (x), as shown in Fig. 4(a)–(d).

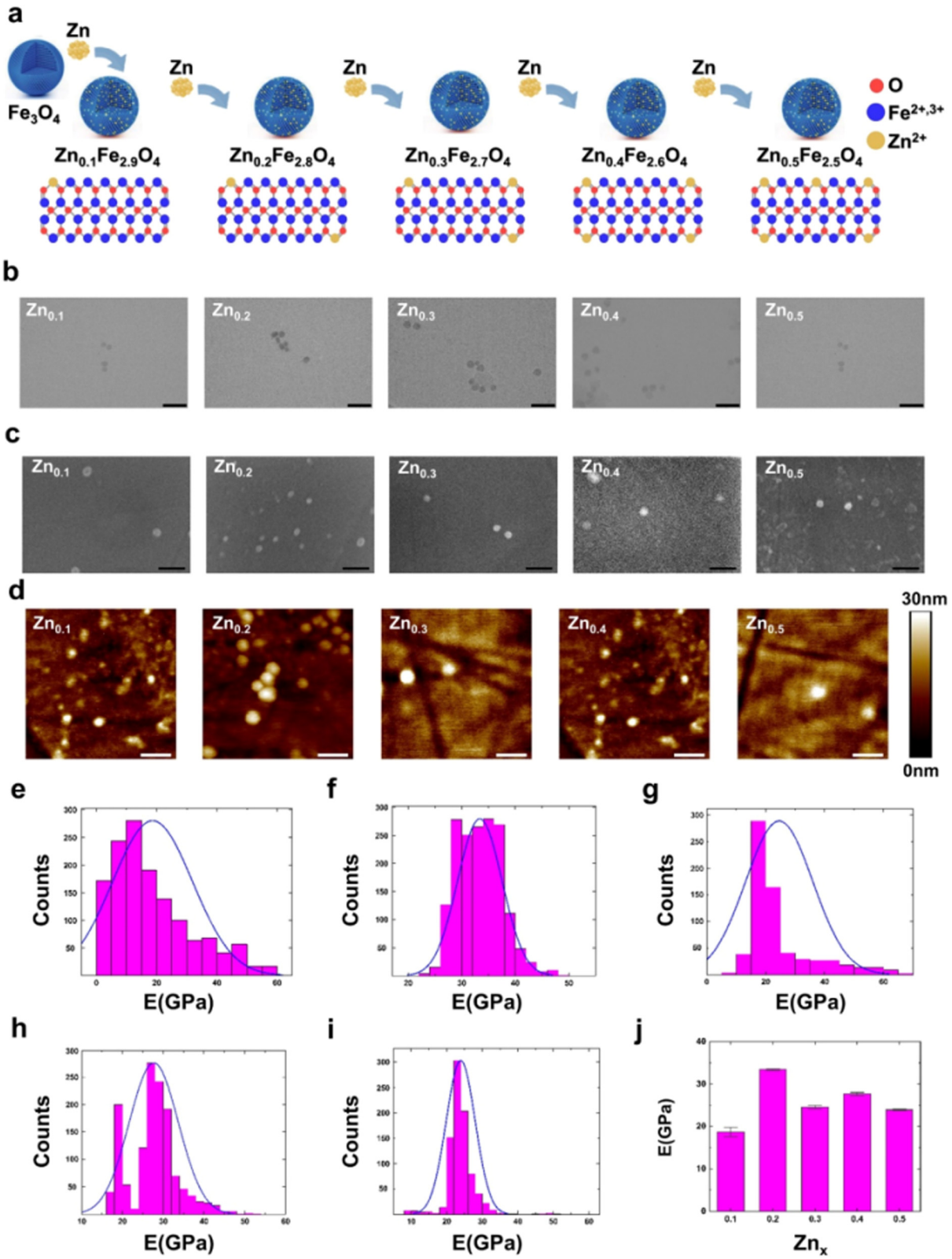

Fig. 2 NPs' stiffness evaluation by single-molecule force spectrometry of atomic force microscopy (SMFS-AFM). (a) Atomic structure of the spinel zinc ferrite changes as the zinc content (x) increases; red, blue, and gold atoms correspond to O, Fe^{2+}, Fe^{3+}, and Zn^{2+} chemical elements, respectively. (b) TEM images of $Zn_xFe_{3-x}O_4$ NPs at different Zn doping contents with scale bars: 50 nm. (c) SEM images at different Zn doping contents with scale bars: 300 nm. (d) The AFM topography images at different Zn doping contents with scale bars: 200 nm. The Gauss distribution of Young's modulus at Zn doping contents (e) x = 0.1, (f) x = 0.2, (g) x = 0.3, (h) x = 0.4, and (i) x = 0.5. (j) The mean Young's modulus (E) values of $Zn_xFe_{3-x}O_4$ NPs at different Zn doping contents.

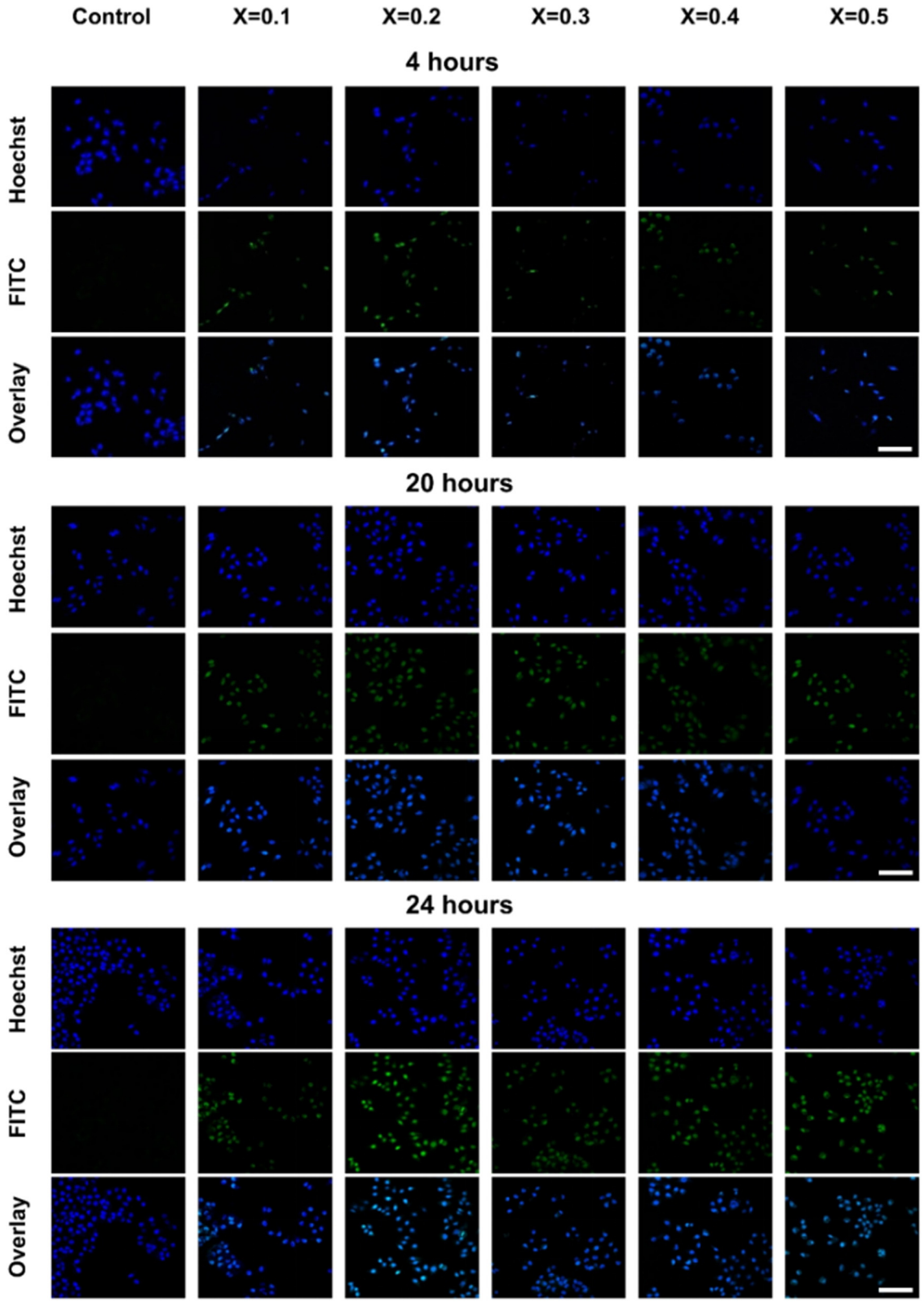

Fig. 3 Confocal microscope MCF-7 cellular uptake of NPs. Confocal microscope images of MCF-7 cells after uptake of different Zn doped content (x = 0.1, 0.2, 0. 3, 0.4 and 0.5) at 4 h, 20 h, and 24 h with a scale bar of 100 μm.

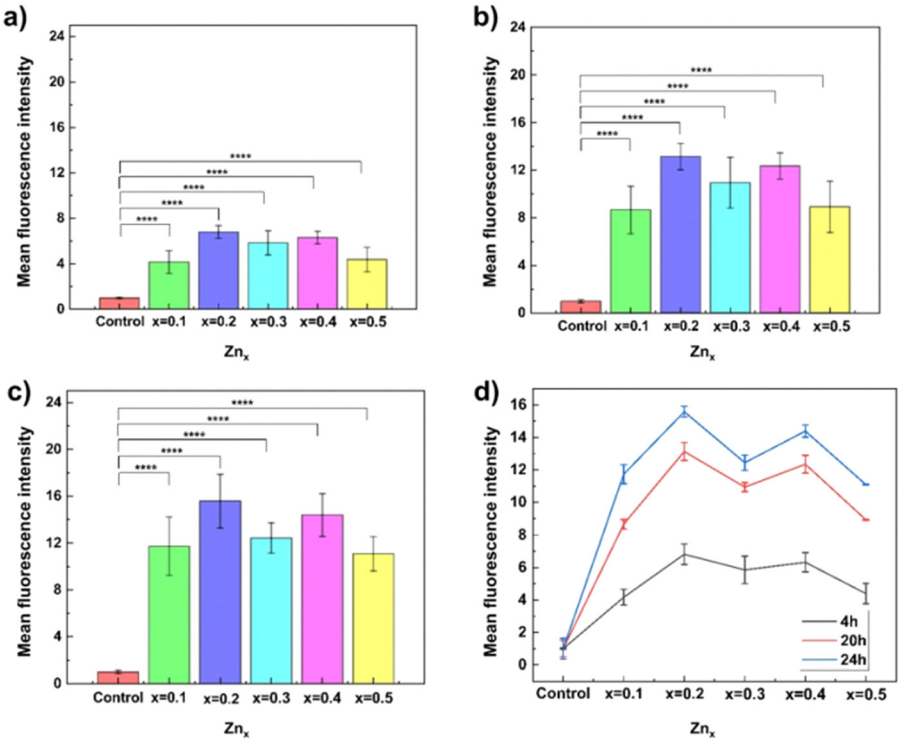

Fig. 4 The mean fluorescence intensity of MCF-7 cells after uptake of different Zn doped content (x = 0.1, 0.2, 0. 3, 0.4, and 0.5) at (a) 4 h, (b) 20 h, and (c) 24 h. (d) The change of the mean fluorescence intensity of MCF-7 cells with increasing Zn doping at different time points (n = 3). * Represents the significance compared with the control. Data are presented as mean ± SD (n = 3). Statistical analysis was performed using a t-test. ****$p < 0.0001$.

3.4 Bio-TEM visualization during NP cellular uptake results and discussion

To better understand the mechanism of the cellular uptake process, MCF-7 intracellular changes and NP localization were visualized using bio-TEM during NP cell uptake. $Zn_xFe_{3-x}O_4$ NPs (x = 0.1, 0.2, 0.3, 0.4, and 0.5) were incubated with MCF-7 cells (50 000 mL^{-1}) for 4, 20, and 24 hours; after incubation, the samples were observed and captured by bio-TEM following infiltration, embedding, slicing, and staining(details can be found in the Materials and Methods section). Fig. 5(d)–(f) show the progress of $Zn_xFe_{3-x}O_4$ NP (x = 0.2) cellular uptake, which has the highest stiffness at 4 h, 20 h, and 24 h, in contrast to Fig. 5(a)–(c) which show the progress of $Zn_xFe_{3-x}O_4$ NP (x = 0.5) cellular uptake, which has a lower stiffness at 4 h, 20 h, and 24 h. A schematic illustration in Fig. 6 shows the cellular uptake of NPs. Bio-TEM images relatively reveal that the stiffer NPs (x = 0.2) exhibit enhanced cellular uptake compared to the softer particles (x = 0.5). Over time, distinct temporal effects become evident. After 4 hours, both stiffer and softer NPs attached with the cell membrane. Remarkably, the observed cellular uptake of NPs was preceded by their accumulation on the cell membrane, indicating that adsorptive endocytosis plays a significant role in the cellular uptake mechanism. After 20 hours, the accumulation of softer NP (x = 0.5) clusters was observed inside the vacuoles near the cell membrane, with an increased accumulation of the stiffer NPs (x = 0.2) particularly in vacuoles and other regions within the lysosome. By 24 hours, NPs appear predominantly in large vacuoles near or within the nuclear wall, with a greater existence observed in the case of stiffer NPs (x = 0.2) compared to softer NPs (x = 0.5). However, in line with previous studies,[66] no evidence of nuclear localization was observed for both types of NPs.

The findings regarding cancerous cellular uptake of NPs exhibited a consistent trend concerning NP stiffness. Stiffer NPs demonstrated higher cellular uptake compared to the softer NPs. Several research studies support our findings, emphasizing the significant role of stiffness in cellular internalization. Rigid lipid-wrapped NPs with high molecular weight polylactic acid showed a higher cellular uptake than soft lipid-wrapped NPs with low molecular weight polylactic acid.[28]

Stiff PLGA–lipid NPs displayed higher cellular uptake in HeLa,[32] BxPC-3 and HPSC[31] than soft PLGA–water–lipid NPs. Macrophages exhibited a higher internalization of stiff nanoparticles (NPs) compared to soft NPs with opsonized microbeads,[67] nanogels,[22] discoidal polymeric nanoconstructs,[34] modified silica nanocapsules,[68] and microparticles derived from tumor-repopulating cells.[23]

Polymer micelles NPs with higher stiffness demonstrated enhanced cellular uptake and deeper penetration within BxPC-3 cells compared to polymer micelles NPs with intermediate rigidity.[18] Stiff monolayer lipid-coated PLGA NPs exhibited superior cellular uptake compared to soft bilayer lipid-decorated PLGA NPs, resulting in higher cytotoxicity towards both HeLa and HUVECs.[30]

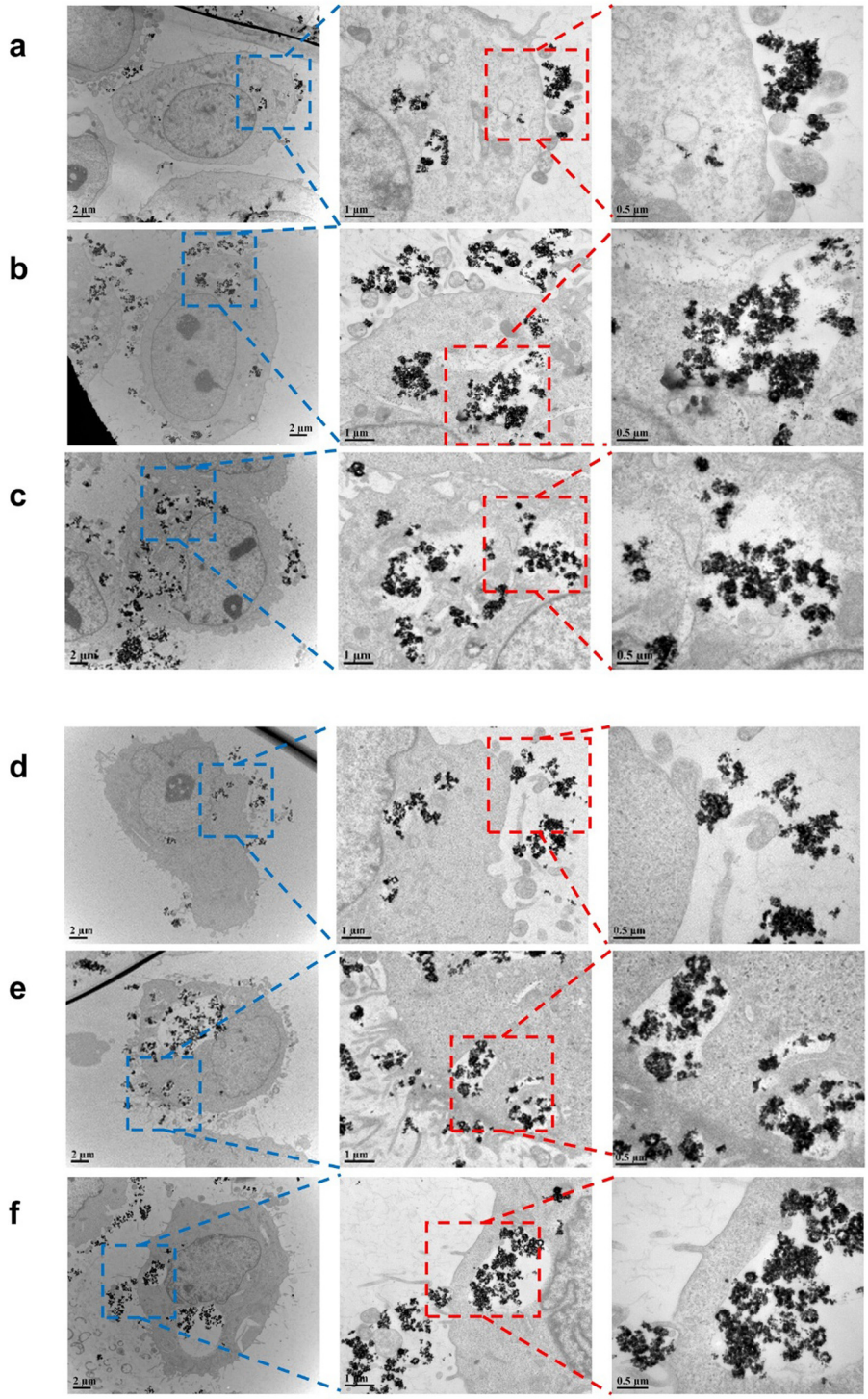

Fig. 5 Bio-TEM visualization during MCF-7 cellular uptake. Bio-TEM images show the progress of $Zn_xFe_{3-x}O_4$ NP (x = 0.5) cellular uptake at (a) 4 h, (b) 20 h, and (c) 24 h with scale bars of 2 μm, 1 μm, and 0.5 μm. Bio-TEM images show the progress of $Zn_xFe_{3-x}O_4$ NP (x = 0.2) cellular uptake at (d) 4 h, (e) 20 h, and (f) 24 hours with scale bars of 2 μm, 1 μm, and 0.5 μm.

The observed effect on cellular absorption was primarily attributed to variations in stiffness, with other mechanical parameters remaining identical including shape, size, and structure. In this study, synthesis of the NPs followed the same steps and conditions, which enabled us to focus on the impact of stiffness on cellular uptake without confounding effects from other mechanical variables. The impact of NP stiffness on cellular uptake is highly dependent on the specific interaction between NPs and cells.[5,7] Various mechanisms that describe the penetration and uptake of NPs have been identified,

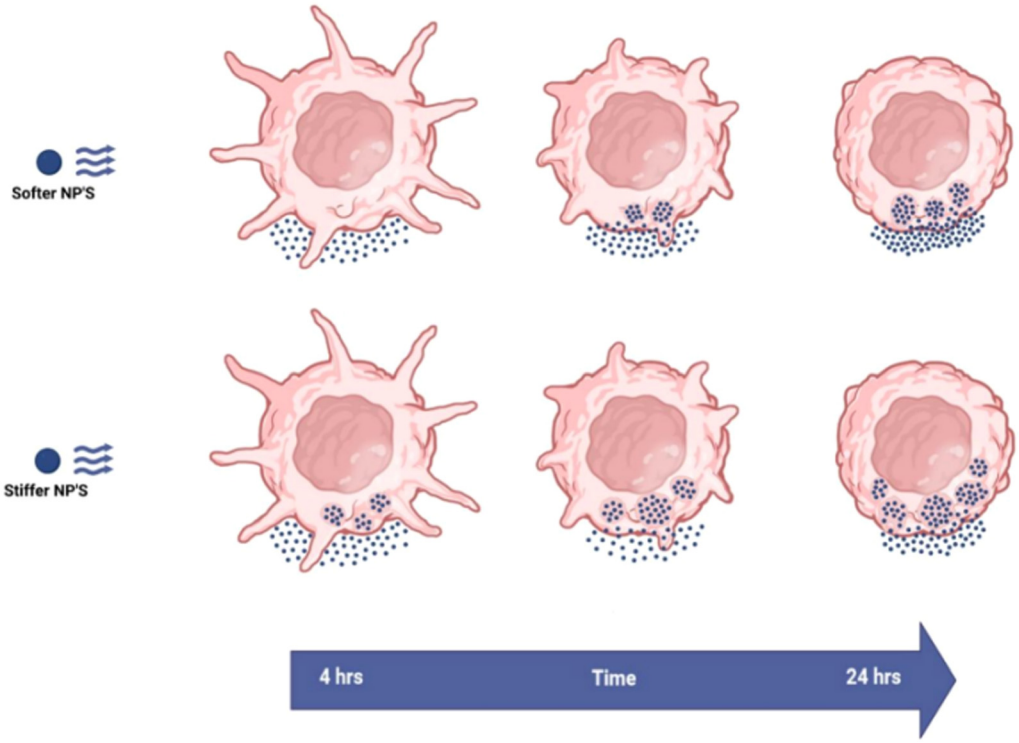

Fig. 6 Bio-TEM visualization during MCF-7 cellular uptake. A schematic illustrating the mechanism of progress of softer and stiffer $Zn_xFe_{3-x}O_4$ NP cellular uptake.

including macrophage phagocytosis and receptor-mediated endocytosis. In the case of stiffer NPs, cancer cells have been found to lose their sensitivity to stiffness through clathrin-mediated endocytosis,[8,32] caveolin-independent endocytosis,[5] and receptor-mediated pathways.[7] Conversely, softer NPs exhibit different modes of penetration, such as fusion[16] and micropinocytosis pathways.[8]

Indeed, NP penetration is significantly influenced by the nature of cancerous cells. NPs are typically internalized by cells through endocytosis,[66] with receptor-mediated endocytosis being a common pathway (stiffer NPs tend to favor this pathway). Although there are exceptions where diffusion becomes the dominant mechanism for NP penetration (softer NPs tend to favor this pathway). For instance, in the case of 3D tumor spheroids, stiffer NPs tend to accumulate in the marginal areas, while softer NPs can penetrate through intercellular spaces.[7]

3.5 Effect of NP stiffness on cellular viability results and discussion

Besides the cellular uptake of NPs by tumor cells, it is crucial to consider the duration of exposure to the NP-delivered drug at a suitable concentration, along with the toxicological characteristics of the drug.[2] Cellular viability was evaluated for different $Zn_xFe_{3-x}O_4$ NPs (x = 0.1, 0.2, 0.3, 0.4, and 0.5) on MCF-7 cells at multiple concentrations (25, 50, 100, 200 μg mL^{-1}) after 4 h, 20 h, and 24 h. In this comprehensive investigation of cellular viability with NPs, we selected 4 hours as the initial time point, corresponding to the onset of observable viability effects at concentrations exceeding 100 μL of NPs. Furthermore, we included a 20 hour time point to examine the temporal influence of cell viability across various concentrations and x-quantities, before the final 24 hour incubation period. The effects of $Zn_xFe_{3-x}O_4$ NPs at different doping contents on MCF-7 cellular viability are depicted in Fig. 7(a)–(c), respectively, regarding different concentrations (50, 100, 200 μg mL^{-1}) with different times points and different doping contents in Fig. 7(d)–(f) and they are further represented in 3D graphs in Fig. 7(g)–(i), respectively.

The cellular viability analysis revealed distinct trends in the cellular uptake of $Zn_xFe_{3-x}O_4$ NPs at different doping contents. $Zn_xFe_{3-x}O_4$ NPs (x = 0.2), in particular, exhibited the lowest viability, whereas $Zn_xFe_{3-x}O_4$ NPs (x = 0.5) demonstrated the highest viability. Cellular viability effects were observed for all NPs after 4 h at a concentration of 100 μg mL^{-1}, except for $Zn_xFe_{3-x}O_4$ (x = 0.5), which showed no effect even at a concentration of 200 μg mL^{-1}. Notably, no effects on cellular viability were observed for all NPs at a concentration of 25 μg mL^{-1} until after 24 h, in which the cellular viability was dramatically decreased time-dependently with different concentrations of $Zn_xFe_{3-x}O_4$ NPs, as presented in Fig. S7(a)–(e) of the ESI.†

The cell viability's time-dependent changes at different concentrations of $Zn_xFe_{3-x}O_4$ NPs are presented in Fig. S7(a)–(e) (ESI†). Similarly, the cellular viability in response to different concentrations for each Zn doping content (x) at 4 h, 20 h, and 24 h is illustrated in Fig. S8(a)–(e)–S10(a)–(e) (ESI†), respectively.

Cellular viability can be referred to as the stress resulting in cells due to the physical presence of NPs on the cell surface

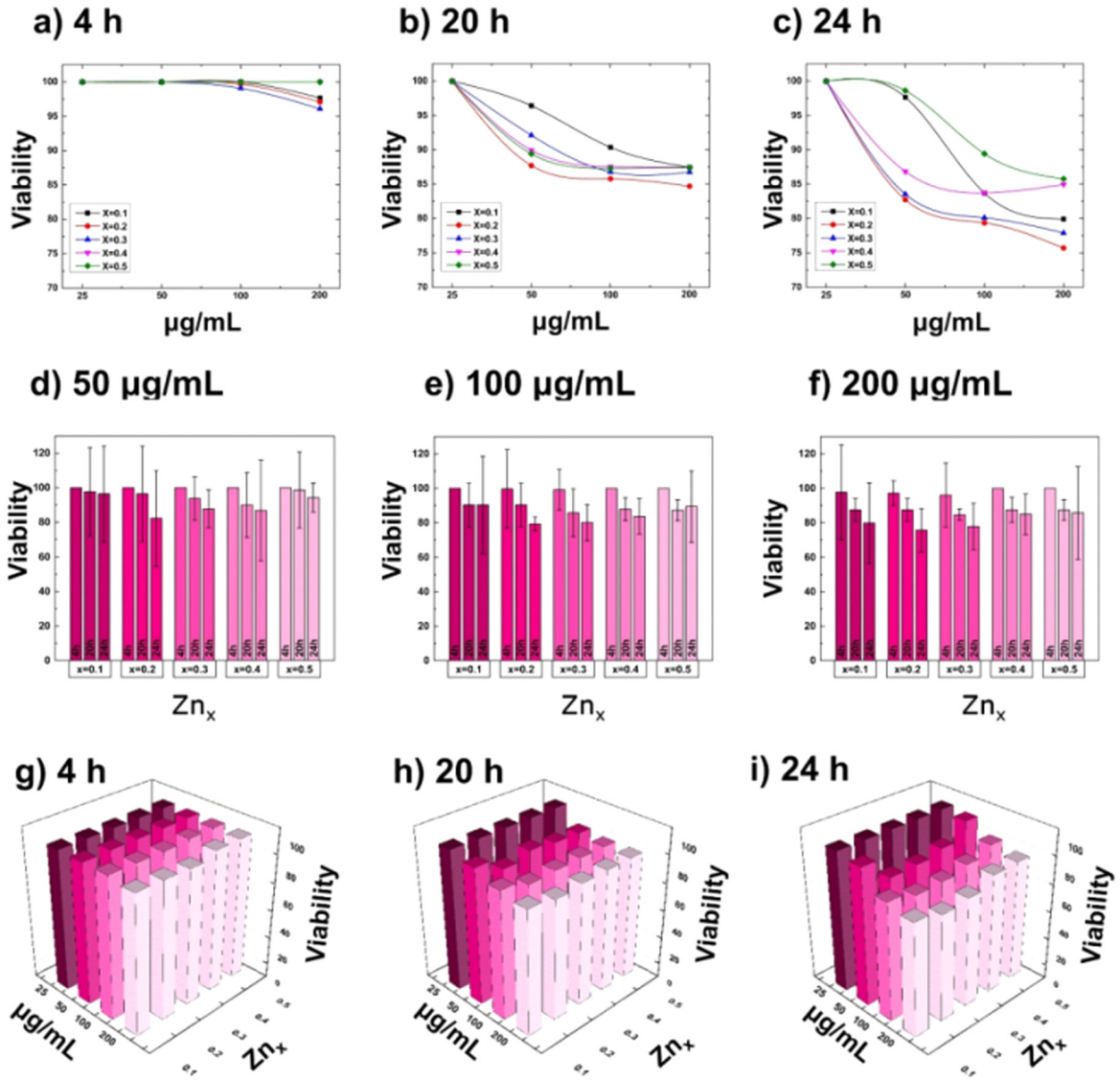

Fig. 7 NP cellular viability on MCF-7 cells. $Zn_xFe_{3-x}O_4$ NP cellular viability on MCF-7 cells at different Zn doped contents (x = 0.1, 0.2, 0. 3, 0.4, and 0.5) and different concentrations (25, 50, 100, 200 μg mL^{-1}) after (a) 4 h, (b) 20 h, and (c) 24 h, n = 3. Cellular viability with different concentrations (d) 50 μg mL^{-1}, (e) 100 μg mL^{-1}, and (f) 200 μg mL^{-1} with different time points and different amounts of doping. 3D graphs representing $Zn_xFe_{3-x}O_4$ NP cellular viability on MCF-7 cells at different Zn doped contents (x = 0.1, 0.2, 0. 3, 0.4, and 0.5) and at different concentrations (25, 50, 100, 200 μg mL^{-1}) after (g) 4 h, (h) 20 h, and (i) 24 h.

rather than the direct NP cytotoxicity.[12] NPs possess various physicochemical characteristics that can impact cellular physiology and directly affect cellular or tissue structure, as well as biocompatibility and toxicity. The cell–NP interaction within variable cellular compartments can disrupt the structural integrity of the cytoskeleton, altering cellular mechanisms and overall cellular functioning.[8] Previous studies[69,70] have demonstrated that these NPs possess an inherent ability to induce apoptosis while exhibiting reduced toxicity toward healthy cells. However, the precise mechanism underlying this behavior remains unclear, although several studies suggest that it is attributed to the selective uptake of NPs.[71]

The study examined zinc-doped NPs at five doping contents, but its scope is limited to low doping contents. Future research should explore higher doping ratios more than x = 5 to better understand the impact of zinc doping on NP stiffness, contributing to the advancement of drug delivery systems and providing nuanced insights. However, it is important to note that the relationship between NP stiffness and cell viability, as an example, is not necessarily deterministic, as the cellular viability process is complex and influenced by various factors, including the physical and chemical properties of NPs, cell types and its characteristics, overall cellular health, and experimental conditions.[9,37,56] We can learn more about *in vivo* biokinetic processes, and make better predictions of potentially harmful responses across the entire body by better comprehending *in vitro* measurements. Apart from the physicochemical properties of NPs, various factors including cell type, size,

incubation parameters, concentration, and measuring methods can affect their cell viability. Therefore, it is essential to exercise caution when interpreting *in vitro* cellular viability results and inferences drawn from them *in vivo*.[10] *In vitro*, investigations often involve delivering a precise dose of NPs into a biological medium containing cells. The subsequent distribution of NPs to cells involves sedimentation and/or diffusion in the liquid media, which can be significantly influenced by the media's composition and the functional coating on the particles, leading to NPs' aggregation and altering cellular absorption kinetics.[9]

4. Conclusion

Efficient NP delivery targeting tumor sites requires a comprehensive understanding of the nanobiological interface for safe design and control over cellular uptake. Mechanobiological measurements are essential to investigate how NPs' mechanical properties affect cell internalization. In this biophysical study, we investigated the NPs' stiffness as a crucial mechanical property and its relationship with the uptake into cancer cells when utilized as drug carriers. Additionally, we measured the cellular viability effects associated with NP uptake. Concisely, using a one-step hydrothermal method, we synthesized five Zn-doping (x = 0.1, 0.2, 0.3, 0.4, 0.5) contents of $Zn_xFe_{3-x}O_4$ NPs. We initially evaluated the stiffness of the zinc-doped NPs at five different doping concentrations utilizing physical and chemical methods. Two different methods have been used for stiffness evaluation: nanoindentation using single-molecule force spectrometry of atomic force microscopy (SMFS-AFM) and chemical structure cations distribution analysis using FTIR and XRD.

The results from the two stiffness methods showed similar patterns, with greater stiffness appearing with Zn-doping at x = 0.2, followed by 0.4, 0.3, and 0.5, and the least stiffness appearing at x = 0.1. These outcomes showed the significant impact of Zn-doping on the mechanical properties of NPs, influencing their biological interaction and efficiency with the targeted cells. Additionally, fluorescence microscopy was used to examine the impact of NP stiffness on their uptake by MCF-7 cells using various Zn-doped concentrations (x) at different time intervals (4 h, 20 h, and 24 h). Bio-TEM was used to examine the intracellular alterations of MCF-7 during the cellular-uptake and the intracellular localization of the NPs with different Zn-doped contents of x = 0.2 and 0.5 at different periods (4 h, 20 h, and 24 h). Furthermore, the cellular viability of $Zn_xFe_{3-x}O_4$ on MCF-7 cells was also evaluated at different Zn-doped contents (x) and different times (4 h, 20 h, and 24 h). The outcomes indicated that both stiffer and softer NPs showed a remarkable adherence to the cellular membrane over time, with adsorptive endocytosis playing a significant role in cellular-uptake. After 20 hours, NPs aggregated near the cell membrane within several vacuoles. It is noteworthy that stiffer NPs demonstrated higher aggregation. By 2 hours, it was seen that NP clusters were predominantly located within large vacuoles close to or inside the nuclear membrane. Interestingly, bio-TEM images showed enhanced penetration for the stiffer NPs (x = 0.2) compared with softer particles (x = 0.5). These findings indicate that NPs' stiffness can significantly impact their cellular uptake and intracellular localization, implicating their therapeutic efficacy and toxicity. Moreover, FITC fluorescence increased in Zn-doped content in MCF-7 cells, indicating enhanced cellular uptake of the NPs over time. A stronger-intensity fluorescence was observed with Zn-doped content x = 0.2, compared to a weaker-intensity fluorescence with x = 0.1. Similarly, the highest toxicity was observed with a Zn-doped content of x = 0.2, while the lowest toxicity was observed with a content of x = 0.5. These results confirm the higher cellular uptake and cellular toxicity of the stiffer NPs over the softer NPs, representing this study's ultimate goal. In summary, this research confirms our previous findings on optimal zinc doping concentrations for MRI contrast applications and the lattice occupancy, magnetic properties, and photothermal effects of $Zn_xFe_{3-x}O_4$ NPs (x = 0.2). Stiffer NPs (x = 0.2) showed a higher cellular uptake than softer NPs. The research provides significant insights into the impact of Zn-doped concentration on the mechanical properties of NPs and how these properties influence the cellular internalization process. Consequently, the study enhances our understanding of the mechanisms involved in cellular uptake and advances the field of drug delivery and cellular transport, ultimately improving the efficiency of NP-based drug delivery.

Conflicts of interest

There are no conflicts to declare.

Acknowledgements

This work was supported by the National Natural Science Foundation of China (32025021, 31971292, 32111540257), the Youth Innovation Promotion Association, Chinese Academy of Sciences (2022301), and the Ningbo 3315 Innovative Talent Project (2018-05-G). Hamzah Al-Madani acknowledges financial support from an ANSO Scholarship for Young Talents.

Notes and references

1 M. Kumar, P. Kulkarni, S. F. Liu, N. Chemuturi and D. K. Shah, *Adv. Drug Delivery Rev.*, 2023, **194**, 114708.
2 Y. H. Cheng, C. L. He, J. E. Riviere, N. A. Monteiro-Riviere and Z. M. Lin, *ACS Nano*, 2020, **14**, 3075–3095.
3 S. Wilhelm, A. J. Tavares, Q. Dai, S. Ohta, J. Audet, H. F. Dvorak and W. C. W. Chan, *Nat. Rev. Mater.*, 2016, **1**, 16014.
4 Y. Takechi-Haraya, Y. Goda, K. Izutsu and K. Sakai-Kato, *Chem. Pharm. Bull.*, 2020, **68**, 473–478.
5 Y. Hui, X. Yi, D. Wibowo, G. Z. Yang, A. P. J. Middelberg, H. J. Gao and C. X. Zhao, *Sci. Adv.*, 2020, **6**, eaaz4316.
6 Y. Takechi-Haraya, Y. Goda and K. Sakai-Kato, *Langmuir*, 2018, **34**, 7805–7812.

7 Y. Hui, D. Wibowo, Y. Liu, R. Ran, H. F. Wang, A. Seth, A. P. J. Middelberg and C. X. Zhao, *ACS Nano*, 2018, **12**, 2846–2857.
8 R. Hartmann, M. Weidenbach, M. Neubauer, A. Fery and W. J. Parak, *Angew. Chem., Int. Ed.*, 2015, **54**, 1365–1368.
9 P. Rees, J. W. Wills, M. R. Brown, C. M. Barnes and H. D. Summers, *Nat. Commun.*, 2019, **10**, 2341.
10 M. T. Zhu, G. J. Nie, H. Meng, T. Xia, A. Nel and Y. L. Zhao, *Acc. Chem. Res.*, 2013, **46**, 622–631.
11 S. K. VanOosten, E. Yuca, B. T. Karaca, K. Boone, M. L. Snead, P. Spencer and C. Tamerler, *Surf. Innov.*, 2016, **4**, 121–132.
12 P. Kielbik, J. Kaszewski, B. Dominiak, M. Damentko, I. Serafinska, J. Rosowska, M. A. Gralak, M. Krajewski, B. S. Witkowski, Z. Gajewski, M. Godlewski and M. M. Godlewski, *Nanoscale Res. Lett.*, 2019, **14**, 373.
13 Y. Liu, Y. X. Li, G. L. Xue, W. X. Cao, Z. L. Zhang, C. M. Wang and X. H. Li, *Acta Biomater.*, 2021, **128**, 474–485.
14 X. Banquy, F. Suarez, A. Argaw, J. M. Rabanel, P. Grutter, J. F. Bouchard, P. Hildgen and S. Giasson, *Soft Matter*, 2009, **5**, 3984–3991.
15 M. R. Yu, L. Xu, F. L. Tian, Q. Su, N. Zheng, Y. W. Yang, J. L. Wang, A. H. Wang, C. L. Zhu, S. Y. Guo, X. X. Zhang, Y. Gan, X. F. Shi and H. J. Gao, *Nat. Commun.*, 2018, **9**, 2607.
16 P. Guo, D. X. Liu, K. Subramanyam, B. R. Wang, J. Yang, J. Huang, D. T. Auguste and M. A. Moses, *Nat. Commun.*, 2018, **9**, 130.
17 H. L. Sun, E. H. H. Wong, Y. Yan, J. W. Cui, Q. Dai, J. L. Guo, G. G. Qiao and F. Caruso, *Chem. Sci.*, 2015, **6**, 3505–3514.
18 T. Stern, I. Kaner, N. L. Zer, H. Shoval, D. Dror, Z. Manevitch, L. Chai, Y. Brill-Karniely and O. Benny, *J. Controlled Release*, 2017, **257**, 40–50.
19 M. Y. Li, X. Y. Jin, T. Liu, F. Fan, F. Gao, S. Chai and L. H. Yang, *Nat. Commun.*, 2022, **13**, 4137.
20 S. M. Kong, D. F. Costa, A. Jagielska, K. J. Van Vliet and P. T. Hammond, *Proc. Natl. Acad. Sci. U. S. A.*, 2021, **118**, e2104826118.
21 Z. G. Teng, C. Y. Wang, Y. X. Tang, W. Li, L. Bao, X. H. Zhang, X. D. Su, F. Zhang, J. J. Zhang, S. J. Wang, D. Y. Zhao and G. M. Lu, *J. Am. Chem. Soc.*, 2018, **140**, 1385–1393.
22 A. C. Anselmo, M. Zhang, S. Kumar, D. R. Vogus, S. Menegatti, M. E. Helgeson and S. Mitragotri, *ACS Nano*, 2015, **9**, 3169–3177.
23 Q. L. Liang, N. N. Bie, T. Y. Yong, K. Tang, X. L. Shi, Z. H. Wei, H. B. Jia, X. Q. Zhang, H. Y. Zhao, W. Huang, L. Gan, B. Huang and X. L. Yang, *Nat. Biomed. Eng.*, 2019, **3**, 729–740.
24 D. Vorselen, M. C. Piontek, W. H. Roos and G. J. L. Wuite, *Front. Mol. Biosci.*, 2020, **7**, 139.
25 B. Ramalingam, T. Parandhaman and S. K. Das, *ACS Appl. Mater. Interfaces*, 2016, **8**, 4963–4976.
26 L. P. Wang, G. Jang, D. K. Ban, V. Sant, J. Seth, S. Kazmi, N. Patel, Q. Q. Yang, J. Lee, W. Janetanakit, S. S. Wang, B. P. Head, G. Glinsky and R. Lal, *Bone Res.*, 2017, **5**, 17051.
27 N. Kol, Y. Shi, M. Tsvitov, D. Barlam, R. Z. Shneck, M. S. Kay and I. Rousso, *Biophys. J.*, 2007, **92**, 1777–1783.
28 B. Eshaghi, N. Alsharif, X. D. An, H. Akiyama, K. A. Brown, S. Gummuluru and B. M. Reinhard, *Adv. Sci.*, 2020, **7**, 2000649.
29 M. Premanathan, K. Karthikeyan, K. Jeyasubramanian and G. Manivannan, *Nanomed.-Nanotechnol.*, 2011, **7**, 184–192.
30 L. Zhang, Q. Feng, J. L. Wang, S. Zhang, B. Q. Ding, Y. J. Wei, M. D. Dong, J. Y. Ryu, T. Y. Yoon, X. H. Shi, J. S. Sun and X. Y. Jiang, *ACS Nano*, 2015, **9**, 9912–9921.
31 Z. Dai, M. R. Yu, X. Yi, Z. M. Wu, F. L. Tian, Y. Q. Miao, W. Y. Song, S. F. He, E. Ahmad, S. Y. Guo, C. L. Zhu, X. X. Zhang, Y. M. Li, X. H. Shi, R. Wang and Y. Gan, *ACS Nano*, 2019, **13**, 7676–7689.
32 J. S. Sun, L. Zhang, J. L. Wang, Q. Feng, D. B. Liu, Q. F. Yin, D. Y. Xu, Y. J. Wei, B. Q. Ding, X. H. Shi and X. Y. Jiang, *Adv. Mater.*, 2015, **27**, 1402–1407.
33 S. H. Yang, D. Heo, J. Park, S. Na, J. S. Suh, S. Haam, S. W. Park, Y. M. Huh and J. Yang, *Nanotechnology*, 2012, **23**, 505702.
34 J. Key, A. L. Palange, F. Gentile, S. Aryal, C. Stigliano, D. Di Mascolo, E. De Rosa, M. J. Cho, Y. Lee, J. Singh and P. Decuzzi, *ACS Nano*, 2015, **9**, 11628–11641.
35 S. Jeon, R. Subbiah, T. Bonaedy, S. Van, K. Park and K. Yun, *J. Cell. Physiol.*, 2018, **233**, 1168–1178.
36 V. Malavé, J. P. Killgore and E. J. Garboczi, *Nanotechnology*, 2019, **30**, 285703.
37 P. del Pino, F. Yang, B. Pelaz, Q. Zhang, K. Kantner, R. Hartmann, N. M. de Baroja, M. Gallego, M. Möller, B. B. Manshian, S. J. Soenen, R. Riedel, N. Hampp and W. J. Parak, *Angew. Chem., Int. Ed.*, 2016, **55**, 5483–5487.
38 H. L. Andersen, B. A. Frandsen, H. P. Gunnlaugsson, M. R. V. Jorgensen, S. J. L. Billinge, K. M. O. Jensen and M. Christensen, *IUCrJ*, 2021, **8**, 33–45.
39 M. A. Islam, A. K. M. A. Hossain, M. Z. Ahsan, M. A. A. Bally, M. S. Ullah, S. M. Hoque and F. A. Khan, *RSC Adv.*, 2022, **12**, 8502–8519.
40 E. H. El-Ghazzawy and M. A. Amer, *J. Alloys Compd.*, 2017, **690**, 293–303.
41 M. B. Mohamed and A. M. Wahba, *Ceram. Int.*, 2014, **40**, 11773–11780.
42 K. V. Chandekar, M. Shkir and S. AlFaify, *J. Mol. Struct.*, 2020, **1205**, 127681.
43 T. Tatarchuk, M. Bououdina, W. Macyk, O. Shyichuk, N. Paliychuk, I. Yaremiy, B. Al-Najar and M. Pacia, *Nanoscale Res. Lett.*, 2017, **12**, 141.
44 M. A. Ali, M. N. I. Khan, M. M. Hossain, F. U. Z. Chowdhury, M. N. Hossain, R. Rashid, M. A. Hakim, S. M. Hoque and M. M. Uddin, *Mater. Res. Express*, 2020, **7**, 036101.
45 M. I. A. A. Maksoud, G. S. El-Sayyad, M. Abd El-Kodous and A. S. Awed, *J. Mater. Sci.: Mater. Electron.*, 2020, **31**, 9726–9741.
46 V. G. Patil, S. E. Shirsath, S. D. More, S. J. Shukla and K. M. Jadhav, *J. Alloys Compd.*, 2009, **488**, 199–203.
47 B. R. Babu and T. Tatarchuk, *Mater. Chem. Phys.*, 2018, **207**, 534–541.

48 T. R. Tatarchuk, N. D. Paliychuk, M. Bououdina, B. Al-Najar, M. Pacia, W. Macyk and A. Shyichuk, *J. Alloys Compd.*, 2018, **731**, 1256–1266.
49 S. M. Patange, S. E. Shirsath, S. P. Jadhav, V. S. Hogade, S. R. Kamble and K. M. Jadhav, *J. Mol. Struct.*, 2013, **1038**, 40–44.
50 K. B. Modi, P. Y. Raval, S. J. Shah, C. R. Kathad, S. V. Dulera, M. V. Popat, K. B. Zankat, K. G. Saija, T. K. Pathak, N. H. Vasoya, V. K. Lakhani, U. Chandra and P. K. Jha, *Inorg. Chem.*, 2015, **54**, 1543–1555.
51 K. V. Chandekar and K. M. Kant, *J. Mol. Struct.*, 2018, **1154**, 418–427.
52 C. Y. Yao, F. Yang, L. Sun, Y. Y. Ma, S. G. Stanciu, Z. H. Li, C. Liu, O. U. Akakuru, L. P. Xu, N. Hampp, H. M. Lu and A. G. Wu, *Nano Today*, 2020, **35**, 100967.
53 Y. Y. Ma, J. B. Xia, C. Y. Yao, F. Yang, S. G. Stanciu, P. Li, Y. H. Jin, T. X. Chen, J. J. Zheng, G. P. Chen, H. X. Yang, L. Q. Luo and A. G. Wu, *Chem. Mater.*, 2019, **31**, 7255–7264.
54 H. Du, F. Yang, C. Y. Yao, Z. C. Zhong, P. H. Jiang, S. G. Stanciu, H. Peng, J. P. Hu, B. Jiang, Z. H. Li, W. H. Lv, F. Zheng, H. A. Stenmark and A. G. Wu, *Small*, 2022, **18**, 2201669.
55 B. Baylis, E. Shelton, M. Grossutti and J. R. Dutcher, *Biomacromolecules*, 2021, **22**, 2985–2995.
56 T. R. Tatarchuk, M. Bououdina, N. D. Paliychuk, I. P. Yaremiy and V. V. Moklyak, *J. Alloys Compd.*, 2017, **694**, 777–791.
57 S. Sharma, D. Kumar, S. Kumar, M. S. Goyat and P. Mandal, *Mater. Chem. Phys.*, 2018, **212**, 292–297.
58 D. Guo, J. N. Li, G. X. Xie, Y. Y. Wang and J. B. Luo, *Langmuir*, 2014, **30**, 7206–7212.
59 F. Nakagomi, P. E. N. de Souza, T. J. Castro, V. K. Garg, A. C. Oliveira, F. C. E. Silva, A. Franco, P. C. Morais and S. W. Silva, *J. Alloys Compd.*, 2020, **842**, 155751.
60 B. P. Rao, B. Dhanalakshmi, S. Ramesh and P. S. V. S. Rao, *J. Magn. Magn. Mater.*, 2018, **456**, 444–450.
61 B. Yang, Z. W. Liu, H. P. Liu and M. A. Nash, *Front. Mol. Biosci.*, 2020, **7**, 00085.
62 S. S. Hafiz, D. Labadini, R. Riddell, E. P. Wolff, M. Xavierselvan, P. K. Huttunen, S. Mallidi and M. Foster, *Part. Part. Syst. Charact.*, 2020, **37**, 1900469.
63 A. Magazzù and C. Marcuello, *Nanomaterials*, 2023, **13**, 963.
64 I. N. Sneddon, *Int. J. Eng. Sci.*, 1965, **3**, 47–57.
65 D. Guo, G. X. Xie and J. B. Luo, *J. Phys. D: Appl. Phys.*, 2014, **47**, 013001.
66 Q. Y. Feng, Y. P. Liu, J. Huang, K. Chen, J. X. Huang and K. Xiao, *Sci. Rep.*, 2018, **8**, 2082.
67 K. A. Beningo and Y. L. Wang, *J. Cell Sci.*, 2002, **115**, 849–856.
68 P.-H. Wu, D. R.-B. Aroush, A. Asnacios, W.-C. Chen, M. E. Dokukin, B. L. Doss, P. Durand-Smet, A. Ekpenyong, J. Guck, N. V. Guz, P. A. Janmey, J. S. H. Lee, N. M. Moore, A. Ott, Y.-C. Poh, R. Ros, M. Sander, I. Sokolov, J. R. Staunton, N. Wang, G. Whyte and D. Wirtz, *Nat. Methods*, 2018, **15**, 491–498.
69 A. Kolodziejczak-Radzimska and T. Jesionowski, *Materials*, 2014, **7**, 2833–2881.
70 M. J. Akhtar, M. Ahamed, S. Kumar, M. A. M. Khan, J. Ahmad and S. A. Alrokayan, *Int. J. Nanomed.*, 2012, **7**, 845–857.
71 G. Bisht, S. Rayamajhi, K. C. Biplab, S. N. Paudel, D. Karna and B. G. Shrestha, *Nanoscale Res. Lett.*, 2016, **11**, 537.